Spatial variation in turbulent heat fluxes in Drake Passage

ChuanLi Jiang *

Sarah T. Gille

Janet Sprintall

Kei Yoshimura

Masao Kanamitsu

Scripps Institution of Oceanography, UCSD

* *Corresponding author address:* ChuanLi Jiang, Scripps Institution of Oceanography, 9500 Gilman Drive, La Jolla, CA 92093-0230. E-mail: chjiang@ucsd.edu

ABSTRACT

High-resolution underway shipboard atmospheric and oceanic observations collected in Drake Passage from 2000 to 2009 are used to examine the spatial scales of turbulent heat fluxes and flux-related state variables. The magnitude of the seasonal cycle of sea surface temperature (SST) south of the Polar Front is found to be twice that north of the Front, but the seasonal cycles of the turbulent heat fluxes show no differences on either side of the Polar Front. Frequency spectra of the turbulent heat fluxes and related variables are red, with no identifiable spectral peaks. SST and air temperature are coherent over a range of frequencies corresponding to periods between 10 hours and 2 days, with SST leading air temperature. The spatial decorrelation length scales of the sensible and latent heat fluxes are 65±3 km and 80±3 km, respectively, comparable to the scale of mesoscale eddies (60 km) in Drake Passage. The scale of the sensible heat flux is consistent with the decorrelation scale for air-sea temperature differences (70±3 km) rather than either SST (153±1 km) or air temperature (138±2 km) alone.

These eddy scales are often unresolved in the available gridded heat flux products. The Drake Passage ship measurements are compared with three recently available higher resolution gridded turbulent heat flux products: the European Centre for Medium-Range Weather Forecasts (ECMWF) high-resolution operational product in support of the Year of Coordinated Observing Modelling and Forcasting Tropical Convection (ECMWF-YOTC), ECMWF interim reanalysis (ERA-INTERIM), and the Drake Passage reanalysis downscaling (DPRD10) regional product. The decorrelation length scales of the air-sea temperature difference, wind speed, and turbulent heat fluxes from these three reanalysis products are significantly larger than those determined from shipboard measurements.

1. Introduction

The Antarctic Circumpolar Current (ACC) is the dominant zonally-oriented flow of the Southern Ocean. It consists of multiple deep-reaching circumpolar jets, which are geostrophic and coincide with sharp frontal gradients in water properties. These narrow fronts separate the Subantarctic water mass to the north from the colder Antarctic water to the south, and are thought to be important for the Subantarctic Mode Water formation and the meridional overturning circulation (Nowlin et al. 1977; Nowlin and Clifford 1982; Orsi et al. 1995; Gille 1999; Rintoul et al. 2001; Sprintall 2003; Lenn et al. 2007). The fronts produce energetic mesoscale eddies and rings (Lutjeharms and Baker Jr. 1980; Daniault and Ménard 1985; Chelton et al. 1990; Gille 1994; Morrow et al. 1994; Gouretski and Danilov 1994) that play an important role in the redistribution of momentum and buoyancy (Bryden 1979; McWilliams et al. 1978; Johnson and Bryden 1989; Ivchenko et al. 1996; Marshall 1997; Gille 1997; Gille et al. 2001; Sprintall 2003).

The Southern Ocean's contribution to the climate system is mediated through air-sea heat fluxes. On the basin-scale, air-sea heat fluxes are important because of their influence on water mass transformation and on the oceanic uptake of heat (e.g. Speer et al. 2000; Dong et al. 2007; Gille 2008). On the eddy-scale O'Neill et al. (2005, 2010) found a simple linear relation between monthly satellite SST anomalies and monthly scatterometer windspeed anomalies in several frontal regions around the global ocean, including the Agulhas Front in the Southern Ocean. Since SST and wind interact in part through air-sea heat fluxes, the existence of a simple relationship between them on small scales implies that small-scale variations in SST and/or wind have the potential to influence air-sea heat fluxes. A number of recent studies have further explored air-sea exchange at fronts (e.g. Small et al. 2008; Cronin et al. 2009), and the net impact of these eddy-scale processes remains an area of active research.

If mesoscale eddies and fronts play an important role in air-sea exchanges, then this implies that air-sea heat flux products need to resolve variations that occur over mesoscale lengthscales. These lengthscales can be short. The first baroclinic Rossby radius L_d, which sets the scale of mesoscale eddies, is estimated be between 10 and 20 km in the Southern Ocean (Chelton et al. 1998). Eddy variability has a wavelength $2\pi L_d$ (e.g. Williams et al. 2007), and correspondingly typical Southern Ocean eddies are between about 60 and 120 km in diameter (e.g. Sprintall 2003; Kahru et al. 2007).

On the other hand, given that atmospheric storm systems can be 500 to 1000 km in diameter, one might wonder whether SST changes on the scale of the Rossby radius can have a substantive impact on basin-averaged air-sea heat fluxes or whether heat fluxes are instead dominated by the large-scale meteorological variations that are resolved in numerical weather prediction (NWP) fields. However, the heat flux data available to evaluate these variations have been very limited both in temporal and spatial resolution. For example, ocean heat flux studies often rely on surface fluxes from NWP reanalyses. These have typically been released at 2^o resolution, so they retain no information on the 10-20 km scale characteristic of the Rossby deformation radius at high-latitudes. At 2^o resolution, the decorrelation scale of the National Centers for Environmental Prediction-National Center for Atmospheric Research (NCEP-NCAR) reanalysis turbulent heat fluxes was found to be around 600 km (Dong et al. 2007), a scale typical of atmospheric storm systems.

At present there is little agreement about the choice of surface flux products for Southern Ocean applications. Surface heat flux products for the Southern Ocean can differ by 50 W m^{-2} (e.g. Dong et al. 2007). Unfortunately, the first lone flux mooring in the Southern Ocean was deployed only in March 2010, in contrast with the tropics which have TOGA-TAO (Tropical Ocean-Global Atmosphere), PIRATA (Pilot Research Moored Array in the Tropical Atlantic), and RAMA (Research Moored Array for African-Asian-Australian Monsoon Analysis and Prediction) moorings. As a result, to date there has been no real opportunity to calibrate or validate gridded flux fields for the Southern Ocean, and especially not to assess their spatial structure.

The paucity of in-situ observations in the Southern Ocean leaves open a host of questions about the true nature of surface fluxes at high latitudes, and our objectives are to address some of these most basic unknown aspects of Southern Ocean air-sea fluxes. We focus specifically on the turbulent fluxes of sensible and latent heat, which depend strongly on air-sea temperature differences and on specific humidity. In our analysis we make use of year-round high-resolution shipboard measurements of the flux-related variables across Drake Passage from 2000 to 2009. Our first objective is to assess the spatial scales over which the turbulent fluxes vary and to ask what physical processes are likely to control small-scale variations in turbulent fluxes.

As part of our analysis, we also compare the shipboard data with NWP flux estimates. New reanalysis efforts offer some prospect for resolving smaller scale features. For example recently the European Centre for Medium-Range Weather Forecasts (ECMWF) released more than two years (May 2008 to present) of data from their high-resolution operational product in support of the Year of Coordinated Observing Modelling and Forcasting Tropical Convection (YOTC) (Waliser and Moncrieff 2008), hereafter referred to ECMWF-YOTC .

Dynamical downscaling (Kanamitsu and Kanamaru 2007) offers another strategy for obtaining small-scale fluxes for specific study regions. Our second objective is thus to evaluate the success of these recent higher resolution NWP products at representing small-scale variations in surface fluxes.

A final objective in assessing spatial scales of variability of surface fluxes is to consider criteria for best observing surface fluxes in the future. High-quality direct observations of turbulent fluxes would be useful for validating future NWP reanalyses of surface fluxes and future satellite-derived turbulent flux fields, and these in situ observations in turn are likely to improve the accuracy of flux products (Bourassa et al. 2010). Before new observing systems are established (whether from ships of opportunity or from moored flux arrays), observing system designers will benefit from knowing not only the wind and temperature conditions that each mooring must withstand, but also appropriate spatial sampling between moorings and critical temporal sampling rates.

The paper is organized as follows. Section 2 describes the shipboard observations, the NWP products, the satellite measurements, and the data interpolation methods used in this study. Section 3 examines the mean difference between the products, the seasonal variability, the length scales of the state variables and their turbulent fluxes, and the spectrum and coherence. The discussion and conclusions are in Section 4.

2. Data

a. Shipboard observations

Shipboard meteorological and near-surface oceanographic parameters were obtained from the R/V Lawrence M. Gould (LMG) which traverses Drake Passage approximately 20 times per year in all seasons. The LMG began providing regular underway atmospheric and oceanic measurements in 2000 and by mid-2009 had completed 202 transects. We retained only the 166 transects that have a northern end point near 55^oS, 65^oW, and we eliminated those transects that fall outside of the Drake Passage triangle with vertices at 65^oW, 55^oS; 65^oW, 62^oS and 57^oW, 62^oS (Fig. 1). We limited our analysis to the region north of 62^oS to avoid regions with persistent wintertime sea ice. For this work, we further narrowed our data set by requiring a relatively constant ship speed so that time series data collected from the ship sensors could be used consistently to infer spatial structure. Of the 166 transects that start or end near point 55^oS,65^oW, about 25 (15%) either did not follow straight trajectories or had a non-constant ship speed (likely due to field work or severe weather). In addition about 33 transects (20%) have big chunks of erroneous data (abnormally noisy measurements, outliers, or missing data) due to sensor malfunction, and about 13 transects (8%) have step-like humidity measurements, especially during the period from 2004 to 2008. Ultimately 95 transects were analyzed for this study, among which there are 47 north-to-south transects and 48 south-to-north transects (Fig. 1).

The LMG takes about two days to complete the open ocean crossing of Drake Passage. Meteorological instruments sample at 1 minute intervals, thus providing about 2880 continuous measurements for each crossing. The shipboard measurements include the upper ocean temperature (4 m below the surface), near surface air temperature (T_{air}), wind speed (U_w), and atmospheric relative humidity, which was converted to specific humidity (q_{air}) using the Buck (1981) algorithm. Dong et al. (2006) showed that there is little bias of the Advanced Microwave Scanning Radiometer-EOS (AMSR-E) ocean temperature (measured at 1-2 mm depth) relative to in-situ temperature measured by the LMG in Drake Passage. The observed ocean temperature is therefore referred to as SST in this study although it is not formally a skin temperature. In this study we used the wind measurements from anemometer at 30 m above the reference waterline on the port side of the ship. Wind measurements were corrected to 10 m using the bulk formulas embedded in the COARE3.0 algorithm (Fairall et al. 1996).

From these shipboard observations of the state variables, the COARE3.0 algorithm is used to calculate the turbulent (latent and sensible) heat fluxes. The COARE3.0 algorithm was developed for wind speeds up to 20 m s^{-1}, in contrast to the earlier COARE 2.5 algorithm which was valid only for wind speeds below 10 m s^{-1}. In the 95 transects that we use, approximately 1% of the ship wind speed data exceed 20 m s^{-1} (and approximately 3% of observations for the 202 total transects since 2000). For latent heat flux, Q_l=ρ_aL$_v$C$_E$U$_w$(q$_{air}$-q$_s$), where ρ_a is the density of air, L$_v$ is the latent heat of evaporation, C$_E$ is the turbulent coefficient of latent heat, and U$_w$ is the 10 m wind speed. The surface specific humidity q$_s$ is calculated from the saturation humidity q$_{sat}$ for pure water at SST, q$_s$=0.98q$_{sat}$(SST), where a factor of 0.98 is used to take into account the effect of a typical salinity of 34 psu. For sensible heat flux, Q_s=ρ_aC$_p$C$_h$U$_w$(SST-θ), where C$_p$ is the specific heat capacity of air at constant pressure, C$_h$ is the turbulent coefficient of sensible heat, and θ is a linear function of air temperature T_{air} (Liu et al. 1979; Yu et al. 2004).

b. NWP products

We compare the shipboard measurements with three recent gridded NWP products: (1) The 3-hourly ECMWF-YOTC state variables and the turbulent heat fluxes from May 2008 to April 2009, which are on a $0.5^o \times 0.5^o$ horizontal grid (Waliser and Moncrieff 2008). We analyze only one year of this product to simplify the reconstruction of the 95 transects (described below); (2) 6-hourly ECMWF reanalysis ERA-INTERIM state variables and turbulent heat fluxes from January 2000 to August 2009, which are on a $1.5^o \times 1.5^o$ horizontal grid (Uppala 2007; Simmons et al. 2007); and (3) hourly Drake Passage reanalysis downscaling (DPRD10) state variables and turbulent heat fluxes on a 10 km$\times$10 km grid that we computed for this study for a 12-month period from 1 May 2008 to 30 April 2009. Note that gridded products (1) and (3) do not cover the full time period covered by the ship measurements.

The DPRD10 is similar to the CARD10 (California Reanalysis Downscaling at 10 km) that was produced for the California current region with some improvement in the boundary conditions and model physics (Yoshimura and Kanamitsu 2009; Kanamitsu et al. 2010). Small-scale features are generated by forcing a high-resolution regional atmospheric model with large-scale NCEP-NCAR reanalysis fields on the domain boundaries. For the California downscaling CARD10, daily SSTs from ECMWF reanalysis ($1^o \times 1^o$) were used (Fiorino 2004; Kanamitsu and Kanamaru 2007). Here, to improve the resolution of the SST forcing in the DPRD10 reanalysis, we employed daily $0.25^o \times 0.25^o$ resolution optimum interpolation

SST analysis Version 2 (Reynolds et al. 2007). This SST product uses both the Advanced Very High Resolution Radiometer (AVHRR) infrared satellite, which has good coverage in cloud-free regions near land, and the AMSR-E satellite, which can see through the year-round clouds in the Southern Ocean. This high resolution SST product was shown to agree with observations (Reynolds and Chelton 2010) and in our tests it improves the small-scale resolving skill in DPRD10 relative to SST from ECMWF reanalysis.

While the SST fields used by NWP products come from independent sources, they are released as part of the NWP products; hereafter they are referred to as ECMWF-YOTC SST, ERA-INTERIM SST, and DPRD10 SST, respectively.

c. Satellite measurements

We also compare the shipboard observations with satellite measurements of SST and winds. For SST we consider the daily $0.25^o \times 0.25^o$ AMSR-E microwave SST product from June 2002 to August 2009 (http://www.ssmi.com). AMSR-E is a multi-channel, multi-frequency, passive microwave radiometer system. It was launched on the National Aeronautics and Space Administration (NASA) Aqua spacecraft on May 4, 2002. It provides sea surface temperature through almost all types of clouds.

For wind we use two products. The first is daily $1^o \times 1^o$ Center for Ocean-Atmospheric Prediction Studies (COAPS) QuikSCAT wind speed from January 2000 to August 2009 (Pegion et al. 2000), hereafter referred to as Q-COAPS. Q-COAPS wind speed at 10 m utilizes a direct minimization approach with tuning parameters determined from Generalized Cross-Validation and QuikSCAT satellite observations filtered by the Normalized Objective

Function (NOF) rain flag. The second wind product is daily $0.25^o \times 0.25^o$ Physical Oceanography Distributed Active Archive Center (PODAAC) Level 3 QuikSCAT wind speed from January 2000 to August 2009, hereafter referred to as Q-PODAAC. Q-PODAAC wind speed determines rain probability by using the Multidimensional Histogram (MUDH) Rain Flagging technique (Huddleston 2000).

d. Constructing transects from gridded products

Gridded products provide synoptic Eulerian maps, while ship transects are not strictly synoptic, because the ship takes approximately two days to cross Drake Passage. To make them comparable, we used linear interpolation to construct 95 transects from each of the six gridded products described in Sections 2b and 2c. Each gridded product was linearly interpolated in longitude, latitude, and time to construct 95 transects representing the same times and locations as the ship sampling. For gridded products that roughly cover the same 10-year period (January 2000 to August 2009) as the ship measurements, such as ERA-INTERIM, Q-COAPS, and AMSR-E (which starts only in June 2002 but is otherwise complete), these 95 transects were constructed to coincide exactly in time with the ship measurements. For gridded products available only for the 12-month period from May 2008 to April 2009 (ECMWF-YOTC and DPRD10), the 95 transects were constructed to match only the day-hour of the ship observations in any individual year, under the assumption that the year-to-year variability in ECMWF-YOTC and DPRD10 has no significant effect on the mean and variance or decorrelation scales. This assumption is re-examined by using a subset of 11 ship transects concurrent with the exact period when ECMWF-YOTC and DPRD10 are available.

3. Results

a. Mean differences and the variance

To evaluate the shipboard data in comparison to gridded NWP and satellite products, we first present the mean differences. In this study, we use the ship-measured state variables and the calculated turbulent fluxes from these variables as reference data. In our discussion, the differences are reported as the NWP or satellite product minus the shipboard measurement.

The ship-derived fluxes are generally thought to be reliable, but there are two issues that could limit their fidelity. First, the relative difference between the wind and the ocean current should be used to calculate the turbulent heat fluxes, and this is effectively what a scatterometer does (Kelly et al. 2001; Bourassa 2006). The impact of the ocean current on the turbulent heat fluxes depends on the ratio of the ocean current component in the direction of the wind to the wind speed itself. In the tropical Pacific near the Intertropical Convergence Zone, where the ocean currents are strong and winds are weak, the ocean currents can have a significant impact on the accuracy of the turbulent heat flux calculation (Kelly et al. 2001; Jiang et al. 2005). In contrast, in the Drake Passage both the ocean currents and the winds are strong. Lenn et al. (2007) found the depth-averaged ocean currents in the Drake Passage are dominantly zonal with velocity speeds of up to 40 cm s^{-1}. Assuming this maximum ocean current occurs at all locations and at all times across Drake Passage, then the maximum influence of the ocean currents is 2.0±0.4 W m^{-2} for latent heat flux, and -0.7±0.4 W m^{-2}

for the sensible heat flux. These upper bounds on errors due to ocean currents are within the uncertainties of the turbulent heat fluxes derived from the in-situ measurements. We also note that NWP products do not take the ocean currents into account in computing wind stress. Therefore, in this study, the effect of the ocean current is not included in the turbulent heat flux calculation. Secondly, as noted above, the COARE 3.0 algorithm was developed for wind speeds up to 20 m s^{-1}, and in the 95 transects we employed here, approximately 1% of the wind speed data exceed this 20 m s^{-1} wind speed limit, with maximum observed winds reaching up to 27 m s^{-1}. In contrast to winds, other flux-related variables are within the tested ranges of the COARE 3.0 algorithm. For instance, within the ensemble of 95 transects, specific humidity values range from 1.4 to 7.3 g kg^{-1}. The air-sea temperature difference (δT=SST-T_{air}) ranges from -6.4^oC to 9.9^oC, and turbulent heat fluxes range from -289.9 to 154.0 W m^{-2}.

The mean differences between the 95-transect averaged turbulent heat fluxes and the flux-related variables are shown in Table 1 (top section). Differences between ship and reanalysis air temperature and air-sea temperature difference are near zero for ECMWF-YOTC and DPRD10, while ERA-INTERIM has a cold bias in air temperature and a warm bias in the air-sea temperature difference (Table 1). The wind speeds of the ERA-INTERIM, DPRD10, and Q-PODAAC are weak compared to the ship measurements. The latent heat flux for the three NWP products are stronger compared to the latent heat flux derived from the ship data, indicating greater heat release from the ocean to atmosphere in the NWP products.

Only 11 ship transects are available during the year for which we consider ECMWF-YOTC and DPRD10 data. To illustrate the effect of the unresolved interannual variability, the bottom section of Table 1 shows mean differences for the 11 ship transects that are coincident in time with the 2008-2009 reanalysis. The smaller number of transects results in larger error bars compared to the mean differences for the averaged 95 transects, and hence the mean differences of the state variables and fluxes of these NWP products are not significantly different, and are also within the accuracy of the ship measurements.

Table 2 shows the standard deviation of the differences between ship data and the reconstructed transects. Standard deviations σ are computed for each transect and values reported are the mean σ and standard error of σ for the full ensemble of 95 transects (top section) or the 11 transects in 2008-2009 (bottom section). The reconstructed NWP and satellite products are much smoother than the ship measurements, especially for the turbulent heat fluxes (Figure 2), and hence their variances are significantly different from the ship measurements (Table 2). Compared to higher resolution NWP products (ECMWF-YOTC and DPRD10), ERA-INTERIM shows smaller variances. AMSR-E SST compares the best with the variability of the ship SST measurement.

The COARE 3.0 algorithm for the turbulent heat fluxes is not identical to the effective bulk flux algorithms used in NWP models. Therefore we plugged the NWP flux-related variables into the COARE 3.0 algorithm to examine the effect of using the COARE 3.0 algorithm on the mean differences and the variability of turbulent heat fluxes. In all cases using the COARE 3.0 algorithm with NWP products (ECWMF-YOTC(C), ERA-INTERIM(C), and DPRD10(C)) results in smaller mean differences than were found from the NWP-derived turbulent heat fluxes. A similar result was reported in the tropical Pacific (Jiang et al. 2005). The smaller mean differences can result from a couple of possible factors. First, the built-in turbulent flux parameterization used by the NWP models can differ substantially from the the COARE 3.0 algorithm (Renfrew et al. 2002; Dong et al. 2007). Secondly, the turbulent heat fluxes from COARE 3.0 algorithm are calculated from 6-hourly averages and not from the state variables computed at each model time step. The effect of using different bulk algorithms might contribute to the magnitude of the fluxes. Use of the COARE 3.0 algorithm did not impact the variability (Table 2). However, it does not contribute to the along-transect standard deviation (Table 2).

b. *Seasonal cycle*

Drake Passage Expendable Bathythermograph (XBT) temperature measurements from the top 100 m of the water column show a distinct seasonal cycle (Sprintall 2003). The temperature tendency and net heat flux (the sum of the shortwave, longwave, and turbulent heat fluxes) in the area-averaged heat budget also show significant seasonal cycles in the Southern Ocean (Sallée et al. 2006; Dong et al. 2007). However, to our knowledge there has been no systematic examination of the seasonality of the turbulent heat fluxes or flux-related state variables using the in-situ measurements in the Drake Passage. We here present the seasonal cycles of the ship-board measurements and the NWP and satellite products.

Fig. 2 shows the time series of the derived turbulent fluxes and the observed flux-related state variables for two transects: one from a warm season (March 2003, solid lines) and one from a cold season (September 2002, dashed lines). Two reconstructed ECMWF-YOTC transects during summer (March 2009) are also shown for comparison. Note that variables in Fig. 2 are plotted as a function of time but could also be plotted as a function of distance. The sea surface temperature and air temperature show a distinct drop from north to south (Fig. 2a) beginning after about 20 hours, indicating the ship's crossing of the Polar Front.

The mean latitude of the Polar Front is around 58.5^{o}S (shaded area in Fig. 1). Wind speed does not show an obvious change at the position of the Polar Front. However, wind speed varies abruptly as a result of storms or gusts, and wind speed variance is higher north of the Polar Front than south (Thompson et al. 2007).

In general March temperatures are warmer than September temperatures (Fig. 3), but the SST gradient is sharper around the Polar Front in September compared to March. Temperatures in March and September are presented here to show the contrast. XBT data show that the temperature drop at the location of the Polar Front is often detectable through at least the top 800 m of the ocean (Sprintall 2003). For the transects shown in Fig. 3, the air-sea temperature difference drops more abruptly across the Polar Front in winter than in summer (Fig. 2d), with correspondingly greater winter sensible heat flux (Fig. 2e). Both summer and winter specific humidity decrease from north to south across the Drake Passage, and the decrease in winter specific humidity is sharper at the front (Fig. 2b). This results in an abrupt increase in winter latent heat flux (Fig. 2e), while summer latent heat flux seems to be closely related to the stronger winds during this transect (Fig. 2c).

Fig. 2 suggests that the state variables and the turbulent heat fluxes both undergo some seasonal variability. To examine their seasonality in detail, we least-squares fitted the 1^o latitude-binned observations to a sinusoidal seasonal cycle. The amplitude of the seasonal cycle of the shipboard sensible (Fig. 4) and latent (Fig. 5) heat fluxes and the flux-related variables vary with latitude (black lines, left panels). The amplitude of the seasonal cycle of SST (Fig. 4a) south of the mean position of the Polar Front (58.5^{o}S) is twice the amplitude north of the front (about 2^{o}C compared to 1^{o}C). The stronger seasonal cycle of SST south of the front is because the SST is influenced by the warm surface water that forms in the austral summer (March to April) on top of the cold Antarctic Surface Water (AASW) in the winter (September to October) (Sprintall 2003). South of the Polar Front, the amplitude of the air temperature and SST seasonal cycles are comparable. In contrast, north of the Polar Front air temperature has a larger seasonal cycle than does SST (Fig. 5a,b). The cause for this is likely related to the much shallower mixed-layer depth south of the Polar Front. None of the other atmospheric variables in Figs. 4 and 5 show the sharp transition in the amplitude of seasonal cycle at the Polar Front, implying that oceanic processes likely govern the seasonal cycle of SST.

The amplitude of the shipboard air-sea temperature difference (δT) seasonal cycle varies from 0.5 to 1.2 ^{o}C (Fig. 4c), but does not show the same latitudinal structure as SST or T_{air}. The amplitude of the seasonal cycle of the sensible heat flux is similar to δT, and ranges from 3 to 21 W m^{-2} (Fig. 4d). The seasonal cycle of the sensible heat flux peaks around 57^{o}S - 58^{o}S, where the Polar Front is located, suggesting that the front likely plays a significant role in the air-sea interaction and the water mass formation in the Southern Ocean.

The amplitude of the seasonal cycle of specific humidity varies from $\sim$ 0.8 g kg^{-1} in the north to $\sim$ 0.6 g kg^{-1} in the south (Fig. 5b). The seasonal cycle of the wind speed is weak compared with the mean wind speed, with an amplitude of less than 1.5 m s^{-1} at all latitudes (Fig. 5a), in agreement with scatterometer winds (Gille 2005). The amplitude of the seasonal cycle of the latent heat flux (Fig. 5c) show a similar magnitude and pattern to the sensible heat flux (Fig. 4d), except for latitudes around the sea ice edge where the latent heat flux shows a slightly smaller amplitude.

In contrast to the amplitudes, the phases of the shipboard turbulent heat fluxes and flux-related variables vary little with latitude (Fig. 4, Fig. 5, black lines, right panels), with the exception of wind speed (Fig. 5a). Wind speed has a small seasonal cycle (within one standard deviation) and can peak at any month of the year. For the different wind products, the phase does not differ significantly within two standard deviations. The SST seasonal cycle peaks mainly in April and May (Fig. 4a), consistent with the upper 100 m XBT temperatures (Sprintall 2003). Both the seasonal cycle of air temperature (Fig. 4b) and specific humidity (Fig. 5b) peak in May, just after the ocean temperature peaks. This provides further evidence to support the hypothesis that the seasonal cycle of ocean temperature is mainly controlled by oceanic processes rather than being driven by atmospheric processes. Unlike SST and air temperature, the air-sea temperature difference peaks from December to January (Fig. 4c). The turbulent heat fluxes peak from May to August, and show a distinct dependence on latitude (Fig. 4d, Fig. 5d).

Compared to the ship measurements, all three NWP products show the same 2^oC amplitude in the seasonal cycle of SST south of the Polar Front; however, they show larger amplitudes north of the front (Fig. 4a). In addition, south of the Polar Front, the amplitudes of the seasonal cycle of air temperature in the NWP data are smaller than in the ship measurements (Fig. 4b). The amplitude of the specific humidity in DPRD10 is smaller than the ship measurements around and south of the Polar Front (Fig. 5b). For the air-sea temperature difference (Fig. 4c) and the turbulent heat fluxes (Fig. 4d, Fig. 5c), the amplitudes of the three NWP products are significantly smaller than the ship measurements around the Polar Front.

c. Temporal and spatial scales

The autocorrelation function (ACF) allows us to determine the predominant temporal and spatial scales over which a variable decorrelates. We compute ACFs as a function of t, where t can be interpreted either as time or along-track distance.

Published studies have used a variety of definitions for determining the decorrelation scale. One simple definition is the time or space lag τ_0 at which the ACF crosses zero. As illustrated in Fig. 6, the first zero crossing (τ_0) is not always a robust indicator of the ACF. In Fig. 6, ACF1 and ACF2 represent the autocorrelation functions for the sensible heat fluxes from ship measurements and ERA-INTERIM, which we will address in more detail below. Although ACF1 and ACF2 have the same zero crossing scales (τ_0), they decorrelate at different rates before crossing zero. The integral scales τ_1 and τ_2 more precisely distinguish ACF1 and ACF2 (Fig. 6). For this study, we therefore use the integral scale, τ, derived by integrating the ACF with respect to the time/space lags from a lag of zero to the first zero crossing, that is, $\tau = \int_0^{\tau_0} \mathrm{ACF} dt$.

Since the ship requires 2 days to traverse the 800 km wide Drake Passage, we used NWP products to evaluate whether variability measured in the ship transects was more representative of spatial or temporal fluctuations. We calculated the temporal and spatial scales directly from the gridded ECMWF-YOTC and ECMWF-INTERIM variables along 65^{o}W without interpolating to the ship tracks. We found that the transect-mean spatial scales along 65^{o}W agree within error bars with the scales calculated from the 95 transects reconstructed along the ship transects from gridded products, while the fixed-position temporal decorrelation scales differed substantially from temporal decorrelation scales inferred from a moving ship position with the NWP data. Therefore, we interpret the decorrelation scales as representing only spatial scales.

The ACFs of SST (Fig. 7a) and air temperature (Fig. 7b) are similar in shape. However, the ACF for air-sea temperature difference (Fig. 7c) drops more abruptly with distance, implying a smaller decorrelation scale. There are no obvious differences between summer and winter ACFs for the flux-related variables, except for SST and the air-sea temperature difference that results in a difference in the sensible heat flux ACF (not shown).

Compared to the ship-derived ACFs, NWP-derived ACFs of air-sea temperature difference (Fig. 7c) and wind speed (Fig. 7e) decrease more slowly, implying much larger decorrelation scales. These long scales appear to translate into long decorrelation scales for latent and sensible heat fluxes (Fig. 7d, g).

Short decorrelation scales indicate small scale variability (or noise). As shown in Fig. 7, the decorrelation scale of the sensible heat flux coincides with the air-sea temperature difference, which is much smaller than either the scale of SST or air temperature. The 95 transect-averaged decorrelation scales of the turbulent heat fluxes and the flux-related state variables from different products are shown in Table 3. The uncertainties in these scales were estimated using a bootstrapping method with 500 subsamples (Diaconis and Efron 1983). Consistent with Fig. 7, the air-sea temperature difference has a much smaller decorrelation scale than either SST or T_{air}, mainly because of the effect of the Polar Front. The front results in a big temperature drop from north to south in both SST and air temperature (e.g., Fig. 2a), but not in the air-sea temperature difference (e.g., Fig. 2d). The shipboard wind speed (72 ± 4km) and the air-sea temperature difference (70 ± 3km) have the smallest decorrelation scales among the four state variables, while SST, T_{air}, and q_{air} all have scales larger than 120 km (Table 3). The decorrelation scales of the latent (80 ± 3km) and sensible (65 ± 3km) heat fluxes are strongly influenced by the shortest scales in the input variables, that is, the wind speed and the air-sea temperature difference.

The decorrelation scales of the satellite products are generally comparable with the shipboard measurements (Table 3 top section). The scale of the spatially gridded AMSRE SST is 160 ± 1 km. The scale of the QuikSCAT wind speed Q-PODAAC is 89 ± 4 km, which is smaller than the scale of Q-COAPS (112 ± 4 km). Both the Q-PODAAC and the DPRD10 wind speeds show scales comparable with the in-situ measurements.

As suggested by Fig. 7, the decorrelation scales of the turbulent heat fluxes and flux-related variables (wind speed and air-sea temperature difference) from the three NWP products are generally larger than the scales derived from in-situ measurements (Table 3 top section). For example, the decorrelation scale of the air-sea temperature difference of ERA-INTERIM is about 41 km larger than that from shipboard measurements, and the scale of ERA-INTERIM wind speed is about 36 km larger. These significant differences in the state variables result in about 32-44 km larger decorrelation scales of the turbulent heat fluxes compared to the ship measurements. Compared to ECMWF-INTERIM, ECMWF-YOTC does a better job at resolving the small-scale variability. The decorrelation scale of the air-sea temperature difference and wind speed of DPRD10 are the smallest among the three recent NWP products (Table 3 top section), which indicates that the high-resolution atmospheric model does indeed show skill in resolving small scales.

To examine the effect of the year-to-year variability in ECMWF-YOTC and DPRD10, the decorrelation scales for the 11 transects with exactly concurrent shipboard and NWP products are shown in Table 3 bottom section. Again the smaller numbers of transects result in larger error bars compared to the averaged 95 transects decorrelation scales (Table 3 top section). However, DPRD10 shows significantly smaller scales in the air-sea temperature difference and turbulent heat fluxes than ECMWF-YOTC, implying that DPRD10 has the potential to resolve small-scale features in the near-surface state variables.

d. High frequency variability

To determine if there is a preferential scale in the higher frequency and wavenumber domain ($<$ 2 days and $<$800 km) in the turbulent heat fluxes and the flux-related variables, we compute frequency/wavenumber spectra (Fig. 8a, b). Furthermore, we calculated the coherence between SST and air temperature in order to examine their interrelations (Fig. 8c, d). We carried out the coherence analysis in two ways: first using the 95 transects ordered temporally in the order the measurements were collected, and second using the 95 transects ordered geographically, with the first record beginning at the northermost point at 55^oS. We found that the temporal ordering produced higher coherence, and therefore results presented here are based on that analysis.

We first compute a time mean as a function of latitude by averaging all transects. From each transect, we then subtract the time mean to obtain a spatially detrended transect, and we apply a fast Fourier transformation. The frequency spectrum is then the sum of the squares of the Fourier components at each frequency divided by 95. In constructing the error bars, each of the 95 transects is treated as an independent realization. This assumption of independence is justifiable because the transects cover all seasons of the year with consecutive transects typically separated in time by 2-6 weeks, and each transect takes about two days to complete.

The spectra of the derived turbulent fluxes and the flux-related variables from shipboard measurements are fairly smooth, except for the high frequencies, in agreement with that suggested for high-resolution spectra by Haren and Gostisux (2009). SST and T_{air} (Fig. 8a) spectra are red except at high frequencies, corresponding to time periods less than 15 minutes. At these highest frequencies the spectra are white, implying the presence of white noise. The slope of the spectra for air temperature is higher than that of the SST, suggesting higher energy at high frequencies for air temperature. Although the shipboard shortwave radiation has a significant diurnal cycle (not shown), there are no significant diurnal peaks in the energy power density of the turbulent fluxes and the other flux-related variables (not shown). Using Argo float temperatures and AMSR-E SSTs, Gille (2009) also found the diurnal cycle to be small in the Southern Ocean.

The slopes of the spectra for the fluxes (not shown) and flux-related variables are very similar to those shown for SST and air temperature (Fig. 8a,b). The power spectral density of sensible heat flux is generally higher than the latent heat flux at all frequencies. Because the reported temporal resolution of ERA-INTERIM, ECMWF-YOTC and DPRD10 variables are 6 hourly, 3 hourly, and hourly, they can only resolve frequencies lower than 2, 4, and 12 cycles per day, respectively.

SST and T_{air} are coherent over a range of frequencies corresponding to periods between $\sim$ 10 hours and 24 hours (Fig. 8c), with SST leading air temperature (Fig. 8d). For the 47 north-to-south transects, SST always leads air temperature for periods between $\sim$ 10 hours and 24 hours. In contrast, for the 48 south-to-north transects, SST always leads air temperature for periods between $\sim$ 12 hours and 16 hours. The phase lag between SST and air temperature at the daily cycle is close to zero (not shown). Similarly, SST and air temperature for all three NWP products are significantly coherent for frequencies < 1 cycle in 12 hours, although the coherence between DPRD10 SST and air temperature drops off more slowly, between 12hour and 6hour time periods (Fig. 8c).

4. Summary

This is one of the first studies to evaluate the small-scale variations in air-sea turbulent heat fluxes near eddies and fronts in the Southern Ocean. The scales of the turbulent heat fluxes and flux-related state variables are evaluated using shipboard measurements from 2000 to 2009 in the Drake Passage. These meteorological observations are unique as the repeat transect provides the only lengthy, year-round time series in the Southern Ocean. These in-situ data are compared against three recent NWP products and two satellite products.

The magnitude of the observed SST seasonal cycle south of the Polar Front is twice that north of the Polar Front. This strong SST seasonal cycle south of the front appears to be associated with the mixed-layer depth variability. In the summer, warm surface water forms on top of the year-round cold AASW, likely resulting in the larger variability of the mixed-layer depth south of the Polar Front. No dependence on latitude was found in other observed variables or in the derived turbulent heat fluxes, which supports the speculation that the ocean physical processes govern the seasonal cycle of SST south of the Polar Front. Frequency spectra of the turbulent heat fluxes and the flux-related variables are red, with no identifiable spectral peaks. The air temperature and SST are coherent for periods between 10 hours and 2 days, with SST leading air temperature.

The decorrelation length scale of the latent heat flux is found to be 80±3 km, and the decorrelation length scale of the sensible heat flux is 65±3 km. These scales appear to co-vary with the smallest scales of the flux-related state variables, that is, the wind speed (72±3 km) and the air-sea temperature difference (70±3 km). This has important implications. First, the scales are consistent with typical Southern Ocean eddies, which are between 60 and 120 km in diameter (Sprintall 2003; Kahru et al. 2007). This finding implies that the mesoscale ocean eddies have the potential to play an important role in the air-sea exchange in the Southern Ocean. Secondly, these scales provide important numbers to evaluate the numerical models used for air-sea interaction studies in the Southern Ocean to gain a better understanding of air-sea interaction mechanisms. The spatial scales of variability of surface fluxes assessed from this study provide useful criteria for best observing surface fluxes in the future. For example, moorings spaced as closely as 65 to 80 km apart are likely to have fully uncorrelated turbulent heat fluxes. Replacing the NWP built-in bulk algorithms with the COARE 3.0 algorithm appears to reduce the differences between the mean turbulent heat fluxes from in-situ data and fluxes from NWP data. However we do not have validation data to assess whether the COARE 3.0 algorithm is more accurate than those built-in to the NWP products, since direct flux observations have not yet been collected in the Southern Ocean.

Compared to the ship measurements, all three recent NWP products show a larger amplitude of SST seasonal cycle north of the Polar Front, which results in a smaller north-south difference in the amplitude of the SST seasonal cycle. The NWP products also show smaller amplitude of the seasonal cycle of air-sea temperature difference and turbulent heat fluxes than the ship measurements near the Polar Front. The spectra of the products are similar to those from ship measurements. Air temperature and SST for the three NWP products are coherent for low frequencies, with air temperature leading SST for ECMWF-YOTC and ECMWF-INTERIM. The NWP products generally lose too much latent heat from the ocean to the atmosphere. Compared to the ship measurements, all three NWP products have larger scales, especially for wind speed, air-sea temperature difference, and turbulent heat fluxes. The satellite SST and windspeed products generally agree more closely with ship data than do the NWP products. Satellite SSTs from AMSRE have a scale comparable to that found in ship measurements, and satellite winds for Q-PODAAC have comparable scales with measured wind speed.

Acknowledgments.

We gratefully acknowledge support from a Scripps Postdoctoral Fellowship (CJ) and from the National Science Foundation (Office of Polar Programs Award 0337998 and OCE Award 0850350). The authors would like to acknowledge Teresa K. Chereskin and Sharon Escher for providing the LMG data sets. ECMWF-YOTC data used in this study have been obtained from the ECMWF data server: http://data-portal.ecmwf.int/data/d/yotc_od/. ERA-Interim data have been obtained from http://data-portal.ecmwf.int/data/d/interim_daily/. AMSRE SST data are produced by Remote Sensing Systems and sponsored by the NASA Earth Science MEaSUREs DISCOVER Project and the AMSR-E Science Team (ftp://ssmi.com/-amsre/). Q-COAPS is downloaded from http://coaps.fsu.edu/scatterometry/gridded/. The Q-PODAAC wind speed data were obtained from the Physical Oceanography Distributed Active Archive Center (PO.DAAC) at the NASA Jet Propulsion Laboratory, Pasadena, CA.

ftp://podaac.jpl.nasa.gov/pub/ocean_wind/quikscat/L3/data.

REFERENCES

Bourassa, M., et al., 2010: High-latitude ocean and sea ice surface fluxes: Requirements and challenges for climate research. *Bull. Amer. Met. Soc.*, submitted.

Bourassa, M. A., 2006: Satellite-based observations of surface turbulent stress during severe weather. *Atmosphere-Ocean Interactions UK: WIT Press*, 35–52.

Bryden, H. L., 1979: Poleward heat flux and conversion of available poential energy in Drake Passage. *J. Mar. Res.*, **37**, 1–22.

Buck, A. L., 1981: New equations for computing vapor pressure and enhancement factor. *J. Appl. Meteorol.*, **20**, 1527–1532.

Chelton, D. B., R. A. deSzoeke, M. G. Schlax, K. E. Naggar, and N. Siwertz, 1998: Geographical variability of the first-baroclinic Rossby radius of deformation. *J. Phys. Oceanogr.*, **28**, 433–460.

Chelton, D. B., M. G. Schlax, D. L. Witter, and J. G. Richman, 1990: Geosat altimeter observations of the surface circulation of the Southern Ocean. *J. Geophys. Res.*, **95**, 17,877–17,903.

Cronin, M.-F., et al., 2009: Monitoring ocean-atmosphere interactions in western boundary current extensions. *Proceedings of the 'OceanObs'09: Sustained Ocean Observations and Information for Society conference*, J. Hall, D. E. Harrison, and D. Stammer, Eds., Venice, Italy, ESA, Vol. 2, publication WPP-306.

Daniault, N. and Y. Ménard, 1985: Eddy kinetic energy distribution in the Southern Ocean from altimetry and FGGE drifting buoys. *J. Geophys. Res.*, **90**, 11,877–11,889.

Diaconis, P. and B. Efron, 1983: Computer-intensive methods in statistics. *Sci. American*, **248**, 116–130.

Dong, S., S. Gille, J. Sprintall, and C. Gentemann, 2006: Validation of Advanced Microwave Scanning Radiometer for the Earth Observing System (AMSR-E) sea surface temperature in the Southern Ocean. *J. Geophys. Res.*, **111 (C04002)**, doi: 10.1029/2005JC002 934.

Dong, S., S. T. Gille, and J. Sprintall, 2007: An assessment of the Southern Ocean mixed-layer heat budget. *J. Climate*, **20**, 4425–4442.

Fairall, C. W., E. F. Bradley, D. P. Rogers, J. B. Edson, and G. S. Young, 1996: Bulk parameterization of air-sea fluxes for Tropical Ocean-Global Atmosphere Coupled-Ocean Atmosphere Response Experiment. *J. Geophys. Res.*, **101 (C2)**, 3747–3764.

Fiorino, M., 2004: A multi-decadal daily sea surface temperature and sea ice concentration data set for the ERA-40 reanalysis. ERA-40 Project Rep. Series 12, ECMWF, Reading, United Kingdom. 16 pp.

Gille, S. T., 1994: Mean sea surface height of the Antarctic Circumpolar Current from Geosat data: Method and application. *J. Mar. Res.*, **99**, 18,255–18,273.

Gille, S. T., 1997: The Southern Ocean momentum balance: Evidence for topographic effects from numerical model output and altimeter data. *J. Phys. Oceanogr.*, **27**, 2219–2232.

Gille, S. T., 1999: Mass, heat, and salt transport in the southeastern Pacific: A Circumpolar Current inverse model. *J. Geophys. Res.*, **104**, 5191–5210.

Gille, S. T., 2005: Statistical characterization of zonal and meridonal ocean wind stress. *J. Atmos. Oceanic Technol.*, **22**.

Gille, S. T., 2008: Decadal-scale temperature trends in the southern hemisphere ocean. *J. Climate*, **21 (18)**, 4749–4765.

Gille, S. T., 2009: Diurnally varying wind forcing and upper ocean temperature: Implications for the ocean mixed layer. *American Meteorological Society Meeting Abstract*.

Gille, S. T., D. P. Stevens, R. T. Tokmakian, and K. J. Heywood, 2001: Antarctic Circumpolar Current response to zonally averaged winds. *J. Geophys. Res.*, **106**, 2743–2759.

Gouretski, V. V. and A. I. Danilov, 1994: Characteristics of warm rings in the African sector of the Antarctic Circumpolar Current. *Deep Sea. Res., Part 1*, **41**, 1131–1157.

Haren, H. V. and V. Gostisux, 2009: High-resolution open-ocean temperature spectra. *J. Geophys. Res.*, **114 (C05005)**, doi: 10.1029/2008JC004 967.

Huddleston, J. N., 2000: Multidimensional Histogram (MUDH) Rain Flag Product Description. *Jet Propulsion Laboratory Version 2.1 (Pasadena)*, CA.

Ivchenko, V., K. Richards, and D. Stevens, 1996: The dynamics of the Antartic Circumpolar Current. *J. Phys. Oceanogr.*, **26**, 753–774.

Jiang, C., M. F. Cronin, K. Kelly, and L. Thompson, 2005: Evaluation of a hybrid satellite-and NWP-based turbulent heat flux product using Tropical Atmosphere-Ocean (TAO) buoys. *J. Geophys. Res.*, **110**, C09 007.

Johnson, G. C. and H. L. Bryden, 1989: On the size of the Antarctic Circumpolar Current. *Deep Sea Res.*, **36**, 39–53.

Kahru, M., B. G. Mitchell, S. T. Gille, C. D. Hewes, and O. Holm-Hanse, 2007: Eddies enhance biological production in the Weddell-Scotia confluence of the Southern Ocean. *Geophys. Res. Lett.*, **34**, doi:10.1029/2007gl030 430.

Kanamitsu, M. and H. Kanamaru, 2007: Fifty-seven-year California Reanalysis Downscaling at 10 km (CaRD10). Part I: System detail and validation with observations. *J. Climate*, **20**, 5553–5571.

Kanamitsu, M., K. Yoshimura, Y.-B. Yhang, and S.-Y. Hong, 2010: Errors of interannual variability and trend in dynamical downscaling of Reanalysis. *J. Geophys. Res.*, **115**, doi:10.1029/2009JD013 511.

Kelly, K. A., S. Dickinson, M. J. McPhaden, and G. C. Johnson, 2001: Ocean currents evident in satellite wind data. *Geophys. Res. Lett.*, **28 (12)**, 2469–2472.

Lenn, Y.-D., T. K. Chereskin, J. Sprintall, and E. Firing, 2007: Mean jets, mesoscale variability and eddy momentum fluxes in the surface layer of the Antarctic Circumpolar Current in Drake Passage. *J. Mar. Res.*, **65**, 27–58.

Liu, W. T., K. B. Katsaros, and J. A. Businger, 1979: Bulk parameterizations of air-sea exchanges of heat and water vapor including molecular constraints at the interface. *J. Atmos. Sci.*, **36**, 1722–1735.

Lutjeharms, J. R. E. and D. J. Baker Jr., 1980: A statistical analysis of the meso-scale dynamics of the Southern Ocean. *Deep Sea. Res., Part 1*, **27**, 145–159.

Marshall, D., 1997: Subduction of water masses in an eddying ocean. *J. Mar. Res.*, **55**, 201–222.

McWilliams, J., W. R. Holland, and J. H. Chow, 1978: A description of numerical Antarctic Circumpolar Currents. *Dyn. Atmos. Oceans*, **2 (3)**, 213–291.

Morrow, R., R. Coleman, J. Bhurch, and D. Chelton, 1994: Surface eddy momentum flux and velocity variances in the Southern Ocean from Geosat altimetry. *J. Phys. Oceanogr.*, **4**, 2050–2071.

Nowlin, W. D. and M. Clifford, 1982: The kinematic and thermohaline zonation of the Antarctic Circumpolar Current at Drake Passage. *J. Mar. Res.*, **40**, 481–507.

Nowlin, W. D., T. Whiteworth III, and R. D. Pillsburry, 1977: Structure and transport of the Antarctic Circumpolar Current at Drake Passage from short-term measurements. *J. Phys. Oceanogr.*, **7**, 778–802.

O'Neill, L. W., D. B. Chelton, and S. K. Esbensen, 2010: The effects of SST-induced horizontal surface wind speed and direction gradients on midlatitude vorticity and divergence. *J. Climate*, 23,255-281.

O'Neill, L. W., D. B. Chelton, S. K. Esbensen, and F. Wentz, 2005: High-resolution satellite measurements of the atmospheric boundary layer response to SST perturbations over the Agulhas Return Current. *J. Climate*, **18**, 2706–2723.

Orsi, A. H., T. Whitworth, and W. D. Nowlin, 1995: On the meridional extent and fronts of the Antarctic Circumpolar Current. *Deep Sea. Res., Part 1*, **42**, 641–673.

Pegion, P., M. Bourassa, D. M. Legler, and J. J. O'Brien, 2000: Objectively-derived daily 'winds' from satellite scatterometer data. *Mon. Wea. Rev.*, **128**, 3150–3168.

Renfrew, I. A., G. W. K. Moore, P. S. Guest, and K. Bumke, 2002: A comparison of surface layer and surface turbulent flux observations over the Labrador Sea with ECMWF and NCEP reanalysis. *J. Phys. Oceanogr.*, **32**, 383–400.

Reynolds, R. W. and D. B. Chelton, 2010: Comparisons of daily sea surface temperature analyses for 2007-2008. *J. Climate*, **23:13**, 3545–3562.

Reynolds, R. W., T. M. Smith, D. B. Chelton, K. S. Casey, and M. G. Schlax, 2007: Daily high-resolution blended analyses for sea surface temperature. *J. Climate*, **20**, 5473–5496.

Rintoul, S., C. Hughes, and D. Olbers, 2001: *The Antarctic Circumpolar Current System.* Academic Press, 271-302 pp.

Sallée, J. B., N. Wienders, K. Speer, and R. Morrow, 2006: Formation of Subantarctic Mode water in the southeastern Indian Ocean. *Ocean Dyn.*, **56**, 525–542.

Simmons, A., S. Uppala, D. Dee, and S. Kobayashi, 2007: The ERA interim reanalysis. *ECMWF Newsletter*, **(110)**, 25–35, Reading, United Kingdom.

Small, R. J., et al., 2008: Air-sea interaction over ocean fronts and eddies. *Dyn. Atmos. Oceans*, **45 (3-4, Sp. Iss. SI)**, 274–319.

Speer, K., S. R. Rintoul, and B. Sloyan, 2000: The diabatic Deacon cell. *J. Phys. Oceanogr.*, **30**, 3212–3222.

Sprintall, J., 2003: Seasonal to interannual upper-ocean variability in the Drake Passage. *J. Mar. Res.*, **61**, 27–57.

Thompson, A. F., S. T. Gille, J. A. MacKinnon, and S. J., 2007: Spatial and temporal patterns of small-scale mixing in Drake Passage. *J. Phys. Oceanogr.*, **37**, 572–592.

Uppala, S. M., 2007: From ERA-15 to ERA-40 and ERA-Interim. *Proc. ECMWF/GEO Workshop on Atmospheric Reanalysis*, Reading, United Kingdom, ECMWF, 17–22.

Waliser, D. and M. Moncrieff, 2008: The YOTC Science Plan. Report WMO/TP 1452, World Meteorological Organization. WCRP No. 130.

Williams, R., C. Wilson, and C. W. Hughes, 2007: Ocean and atmosphere storm tracks: the role of eddy vorticity forcing. *J. Phys. Oceanogr.*, **37**, 2267–2289, doi:10.1175/JPO3120.1.

Yoshimura, K. and M. Kanamitsu, 2009: Specification of external forcing for regional model integrations. *Mon. Wea. Rev.*, **137**, 1409–1421.

Yu, L., R. A. Weller, and B. Sun, 2004: Improving latent and sensible heat flux estimates for the Atlantic Ocean (1988–99) by a synthesis approach. *J. Climate*, **17**, 373–393.

List of Tables

Table 1. Mean and the standard error of 95-transect averaged (top section) and 11-transect averaged (bottom section) turbulent fluxes and flux-related state variables from the ship measurements (row 1). The standard error equals the standard deviation divided by square root of the number of the observations (95 or 11). Bias and standard error of the difference of transect averaged seven state variables from ECMWF-YOTC, ERA-INTERIM, DPRD10, Q-COAPS, Q-PODAAC, and AMSR-E relative to ship measurements (rows 2-7). Bias and standard error of the difference of the turbulent heat flux estimations from ECMWF-YOTC, ERA-INTERIM, and DPRD10 using COARE 3.0 algorithm (rows 8-10).

	SST ^{o}C	T_{air}, ^{o}C	δT, ^{o}C	q_{air}, g kg^{-1}	U_{w}, m s^{-1}	Q_{l}, W m^{-2}	Q_{s}, W m^{-2}
95-transect averaged							
Ship	2.7±0.2	2.9±0.3	-0.2±0.2	4.1±0.1	9.7±0.5	-17.7±3.3	1.4±3.2
ECMWF-YOTC	-0.1±0.1	-0.2±0.3	0.1±0.3	-0.1±0.1	-0.5±0.6	-6.0±4.7	1.8±3.9
ERA-INTERIM	-0.1±0.1	-0.3±0.1	0.2±0.1	-0.1±0.0	-0.9±0.4	-4.4±1.9	-0.4±1.9
DPRD10	0.1±0.1	-0.0±0.3	0.1±0.3	-0.1±0.1	-0.7±0.6	-9.3±4.5	3.6±3.8
AMSR-E	-0.0±0.1						
Q-COAPS					-0.4±0.5		
Q-PODAAC					-1.4±0.5		
ECMWF-YOTC(C)						-5.5±4.6	1.1±3.9
ERA-INTERIM(C)						-1.5±1.8	-0.3±1.9
DPRD10(C)						-1.5±4.3	2.3±3.7
11-transect averaged							
Ship	2.7±0.4	3.4±0.5	-0.7±0.5	10.8±1.1	4.2±0.2	-16.0±8.9	7.2±6.8
ECMWF-YOTC	-0.2±0.2	-0.8±0.4	0.6±0.3	-1.1±1.1	-0.4±0.1	-10.8±5.2	7.4±6.3
DPRD10	0.0±0.3	-0.4±0.5	0.4±0.5	-1.5±1.3	-0.1±0.2	-10.2±7.9	0.2±7.5
ECMWF-YOTC(C)						-10.3±5.1	-5.6±5.4
DPRD10(C)						-1.8±7.7	-1.2±7.3

Table 2. Standard deviation of 95-transect averaged (top section) and 11-transect averaged (bottom section) turbulent fluxes and flux-related state variables from the ship measurements (row 1). Here standard deviation, σ, is computed for each transect, and reported values represent the mean and standard error of σ for the ensemble of transects. Variables are as specified in Table 1

.

	SST ^{o}C	T_{air}, ^{o}C	δT, ^{o}C	q_{air}, g kg^{-1}	U_{w}, m s^{-1}	Q_{l}, W m^{-2}	Q_{s}, W m^{-2}
95-transect averaged							
Ship	2.2±0.4	2.1±0.6	1.1±0.4	0.6±0.2	2.9±0.9	19.3±9.8	15.7±8.1
ECMWF-YOTC	0.7±0.2	1.2±0.5	1.3±0.5	0.5±0.3	3.6±1.2	27.2±13.7	19.9±9.3
ERA-INTERIM	0.7±0.2	0.8±0.2	0.9±0.2	0.2±0.1	2.2±0.8	13.6±6.4	12.6±5.8
DPRD10	0.8±0.2	1.3±0.5	1.3±0.5	0.6±0.2	3.6±1.1	28.5±11.1	20.8±9.2
AMSR-E	0.5±0.1						
Q-COAPS					2.6±0.8		
Q-PODAAC					3.1±1.1		
ECMWF-YOTC(C)						26.4±12.9	20.0±9.4
ERA-INTERIM(C)						13.6±6.2	12.9±5.7
DPRD10(C)						26.1±10.9	20.2±9.3
11-transect averaged							
Ship	2.3±0.5	2.3±0.3	1.0±0.4	0.6±0.2	2.7±1.0	20.1±10.8	15.8±7.7
ECMWF-YOTC	0.7±0.2	1.2±0.5	1.2±0.5	0.5±0.3	3.4±1.2	26.6±14.0	19.4±9.3
DPRD10	0.7±0.2	1.0±0.4	1.0±0.5	0.5±0.2	2.9±0.9	35.3±15.0	20.2±7.5
ECMWF-YOTC(C)						15.3±6.9	12.9±4.6
DPRD10(C)						20.5±9.2	16.2±8.4

TABLE 3. Decorrelation scales (in kilometers) for 95-transect averaged (top section) and 11-transect averaged (bottom section) SST, air temperature T_{air}, specific humidity q_{air}, 10 m wind speed U_w, air-sea temperature difference SST-T_{air}, latent heat flux Q_l, and sensible heat flux Q_s. Error bars are one standard deviation of 500 subsamples using a bootstrapping method.

	SST	T_{air}	q_{air}	U_w	SST-T_{air}	Q_l	Q_s
95-transect averaged							
Ship	153±1	138±2	124±4	72±4	70±3	80±3	65±3
ECMWF-YOTC	165±1	152±2	130±4	92±3	105±4	111±4	96±4
ERA-INTERIM	165±1	151±2	135±3	108±3	111±3	112±3	109±4
DPRD10	163±1	153±2	117±3	85±3	96±3	100±4	94±3
AMSRE	160±2						
Q-COAPS				112 ± 4			
Q-PODAAC				89 ± 4			
11-transect averaged							
Ship	159±3	147±5	145±7	63±8	60±7	98±9	59±10
ECMWF-YOTC	166±3	156±8	152±8	88±7	100±9	125±12	95±11
DPRD10	164±3	160±3	129±8	85±12	74±9	98±13	68±9

List of Figures

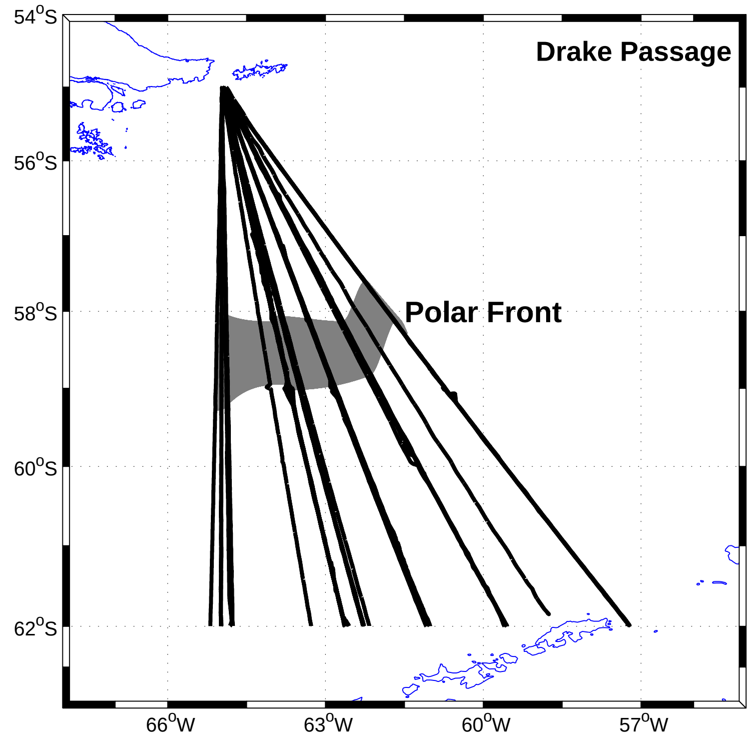

FIG. 1. The cruise tracks of 95 LMG transects (black lines) in the Drake Passage from 2000 to 2009. The shaded area shows the position of the Polar Front determined from XBT observations with its standard deviation (Sprintall 2003). Note that the mean Polar Front is located around 58.5 ^{o}S.

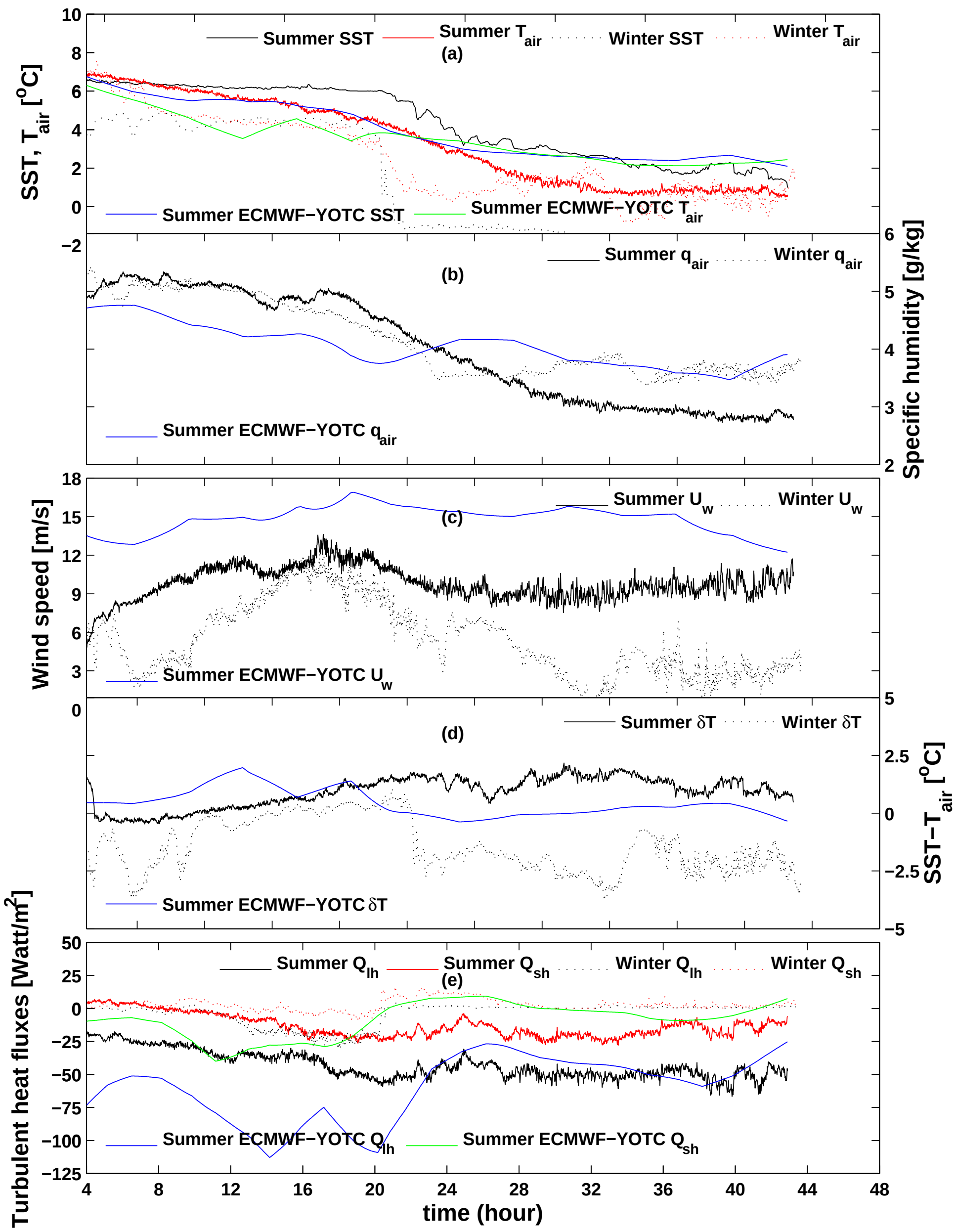

FIG. 2. Time series of (a) SST and T_{air} (^{o}C), (b) specific humidity q_{air} (g kg^{-1}), (c) 10 m wind speed U_w (m s^{-1}), (d) air-sea temperature difference δT = SST-T_{air} (^{o}C), and (e) latent heat flux Q_l and sensible heat flux Q_s (W m^{-2}) for two transects in a typical summer (March 2003, solid lines) and a typical winter (September 2002, dotted lines). Black and red lines are for ship measurements. Blue and green lines are for ECMWF-YOTC reconstructed transect in a typical summer (March 2009). The x-axis shows the time (hour) of the transect with $t = 0$ at the north end point 65^{o}W, 55^{o}S to $t = 44$ hour at the southern point 62^{o}S.

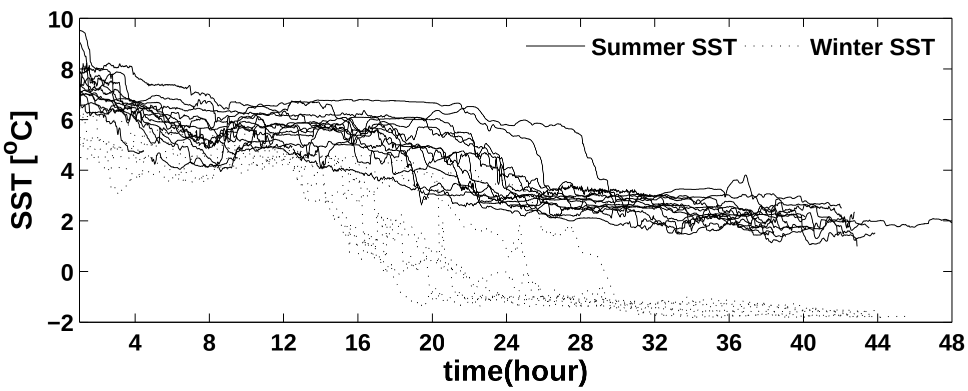

FIG. 3. Time series of SST (^{o}C) of all late summer (March, solid lines) and late winter (September, dotted lines) transects. The x-axis shows the time (hour) of the transect with $t = 0$ at the north end point 55^{o}S to $t = 44$ hours at the southern point 62^{o}S.

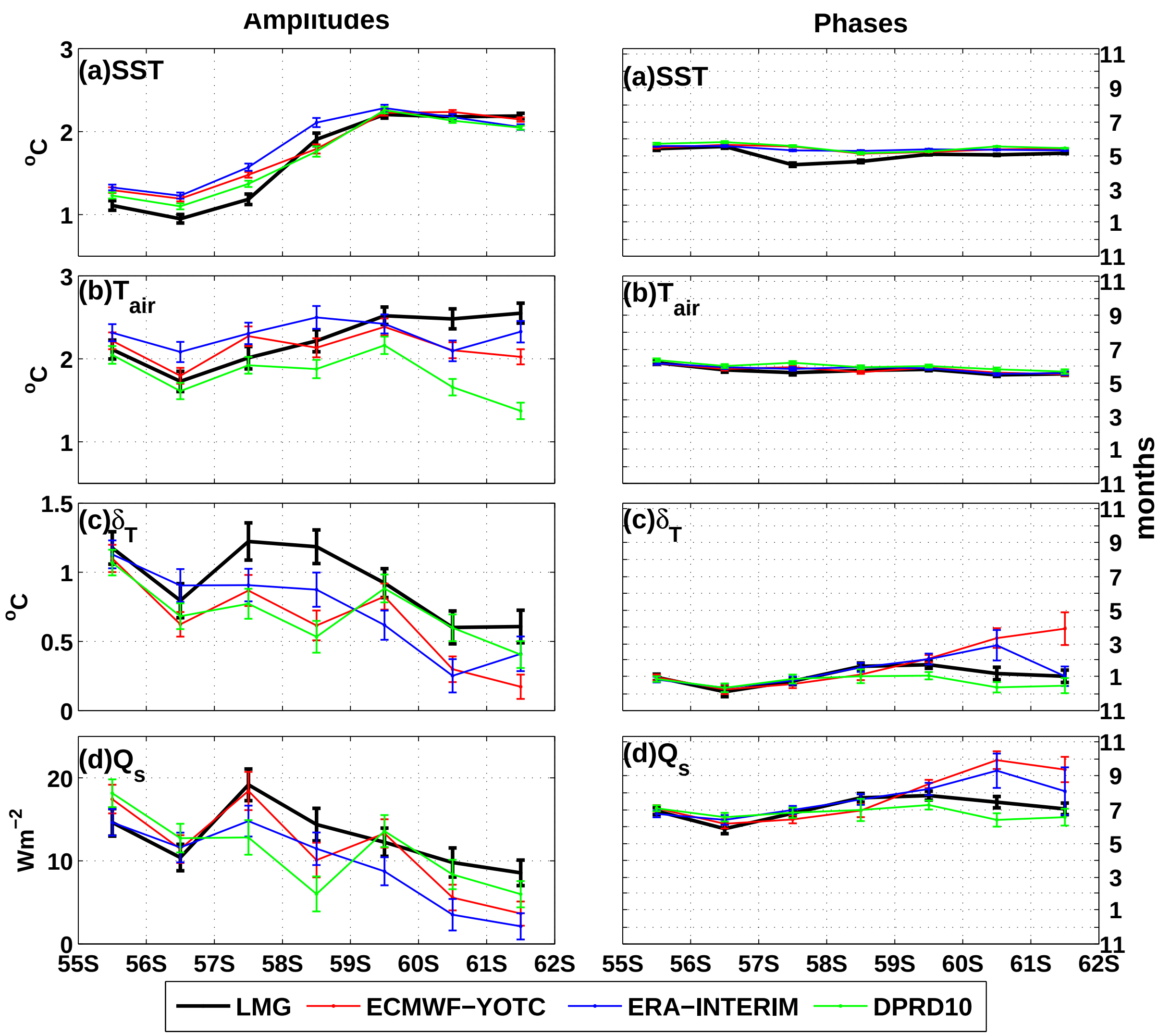

FIG. 4. The amplitudes (left panel) and phases (right panel) of the seasonal cycles of the sensible heat fluxes (Q_s) and the flux-related variables: (a) SST, (b) T_{air}, (c) air-sea temperature difference δT, and (d) sensible heat flux Q_s. Error bars denote the standard error of the means (N=95).

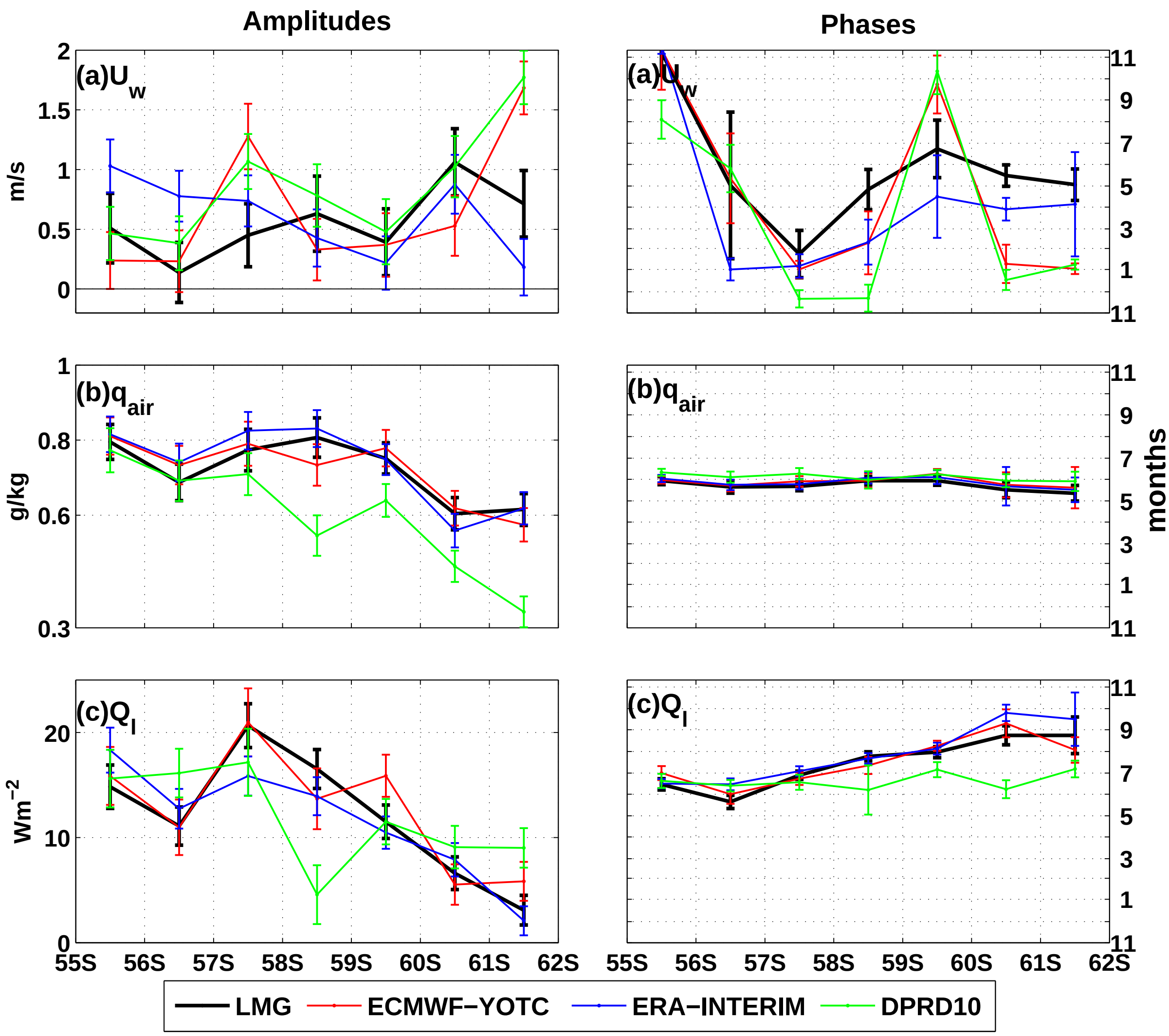

FIG. 5. The amplitudes (left panel) and phases (right panel) of the seasonal cycles of the latent heat fluxes (Q_l) and the flux-related variables: (a) wind speed U_w, (b) air specific humidity q_{air}, and (c) latent heat flux Q_l. Error bars denote the standard error of the mean (N=95).

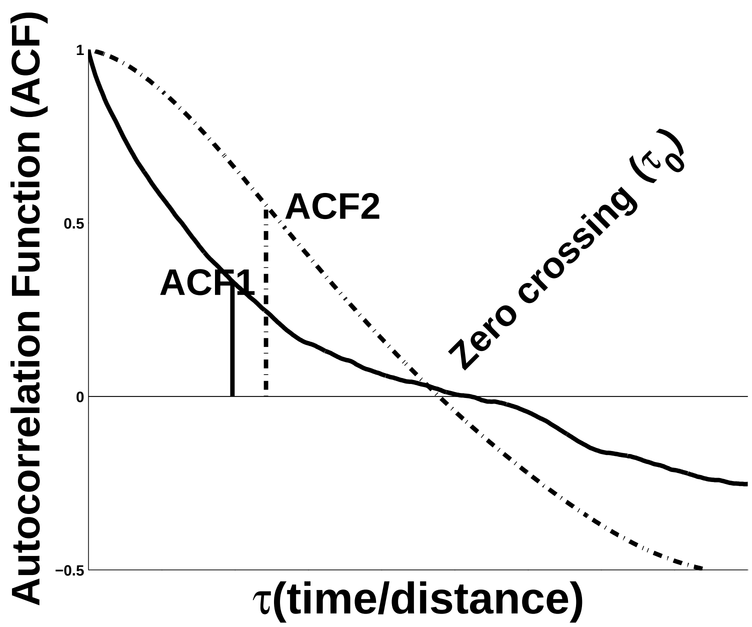

Fig. 6. Definition of the decorrelation scales: integral time scales. Note that ACF1 and ACF2 have the same zero crossing scales (τ_0), but their integral time scales τ_1 and τ_2 precisely measure how ACFs change on small-scales. ACF1 and ACF2 represent the autocorrelation functions for the sensible heat fluxes from ship measurements and ERA-INTERIM.

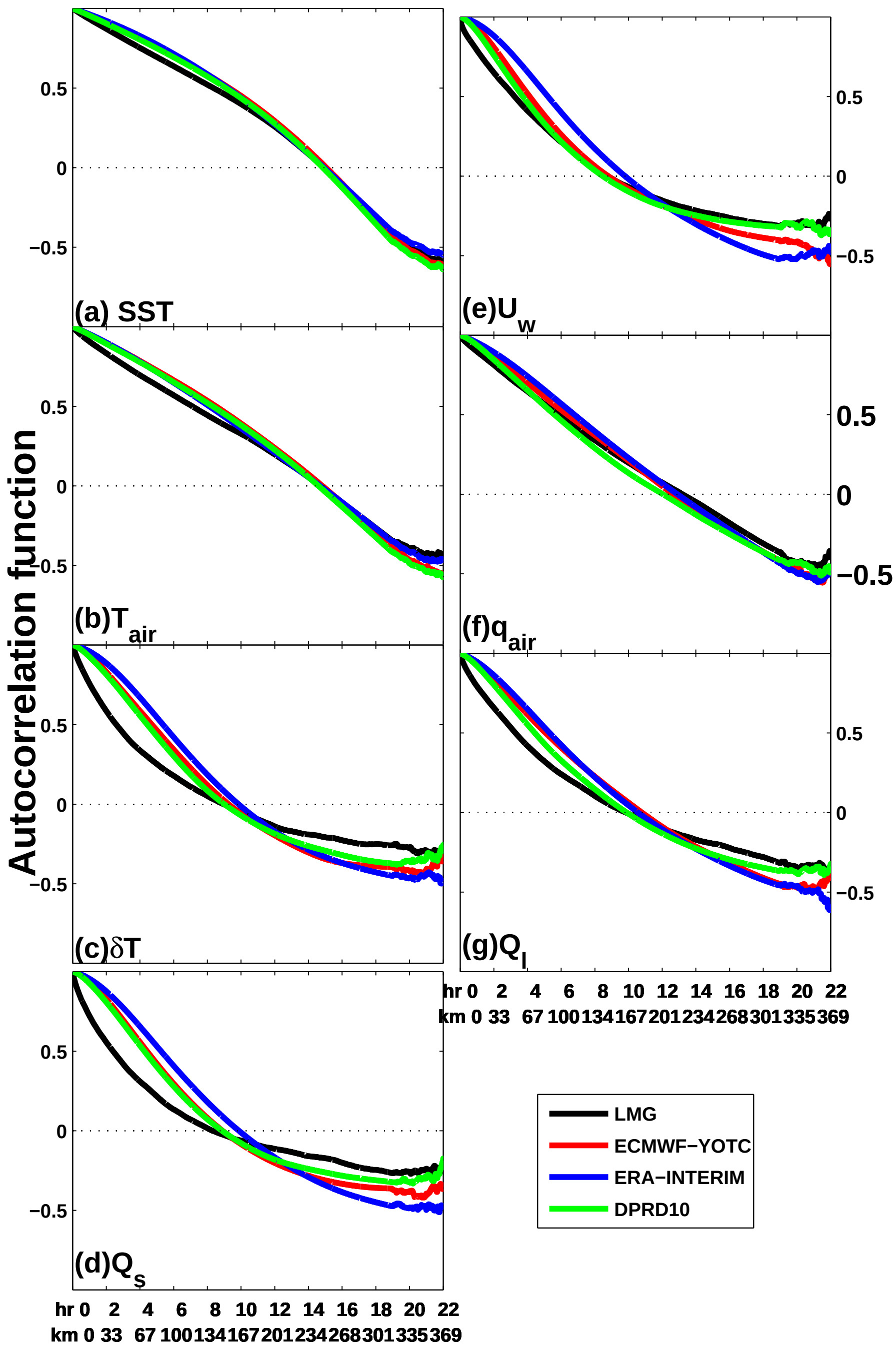

FIG. 7. Autocorrelation functions for (a) SST (^{o}C), (b) air temperature T_{air} (^{o}C), (c) air-sea temperature difference δT=SST-T_{air} (^{o}C), (d) sensible heat flux Q_s (W m^{-2}) (left panel from top to bottom), (e) wind speed U_w (m s^{-1}), (f) air specific humidity q_{air} (g kg^{-1}), and (g) latent heat flux Q_s (g kg^{-1}) (right panel from top to bottom) for LMG (black), ECMWF-YOTC (red), ERA-INTERIM (blue), and DPRD10 (green).

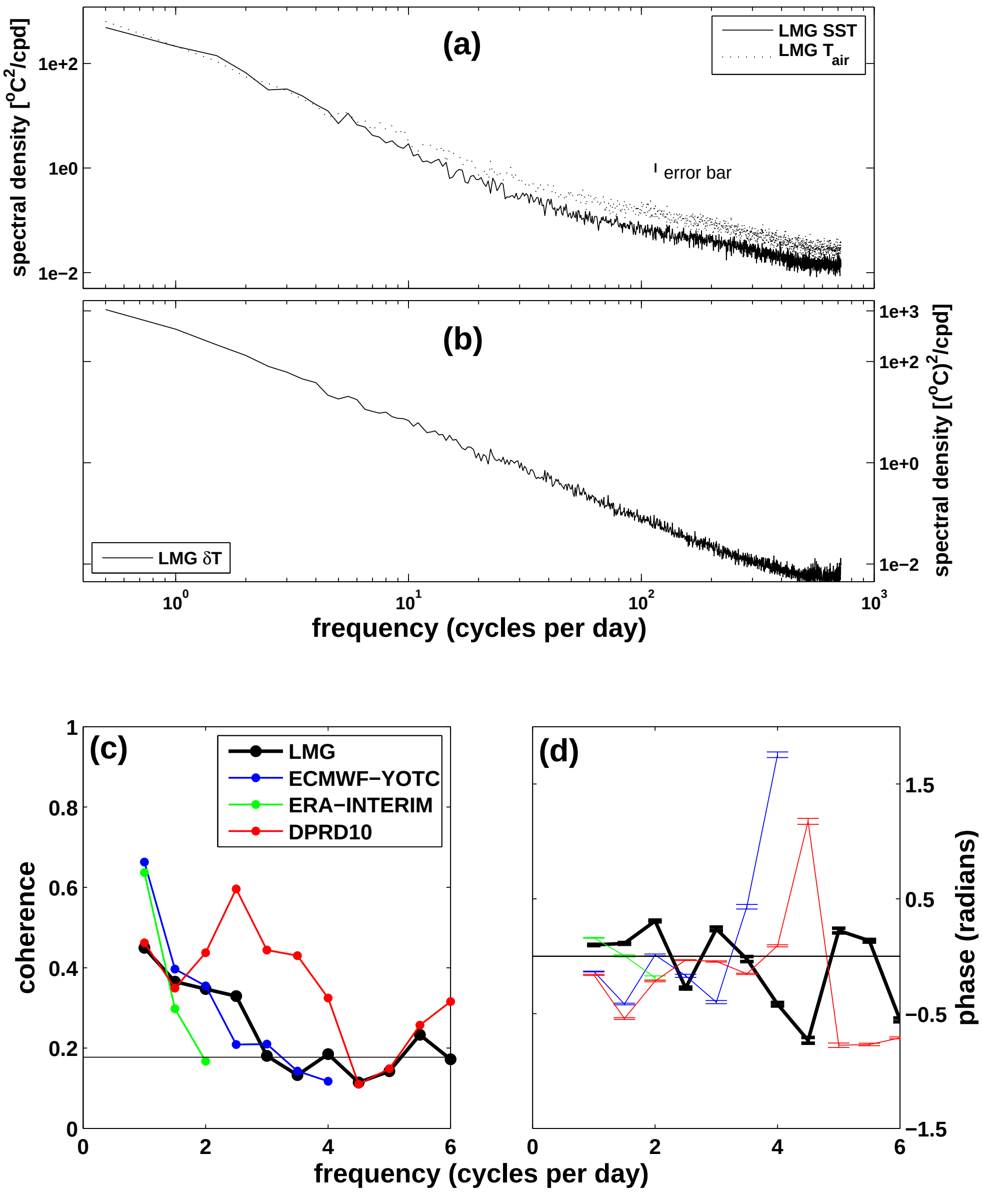

FIG. 8. The power spectrum of (a) SST and air temperature T_{air} (^{o}C), and (b) air-sea temperature difference δT =SST-T_{air} (^{o}C). The (c) coherence of SST and air temperature, and (d) phase difference between SST and air temperature. Negative phase difference indicates air temperature leads SST. The black line in (c) shows the 95 % significance level.